Ceramics International xxx (xxxx) xxx

Contents lists available at ScienceDirect

Ceramics International

journal homepage: www.elsevier.com/locate/ceramint

The influence of Ca^{2+} and Zn^{2+} doping on the development of sustainable pigments based on $GdFeO_3$ perovskite: From a reddish colour towards a pure black

Maria Fortuño-Morte, Pablo Serna-Gallén, Héctor Beltrán-Mir *, Eloísa Cordoncillo **

Departamento de Química Inorgánica y Orgánica, Universitat Jaume I, Av. Vicent Sos Baynat s/n, 12071, Castelló, Spain

ARTICLE INFO

Keywords:
Perovskite
Black pigment
Environment-friendly
Coprecipitation

ABSTRACT

Black pigments are very commonly used and arouse widespread interest in the ceramic industry. Nevertheless, these pigments contain toxic elements that are detrimental to human health. In view of this, the present work is focused on the development of sustainable black pigments prepared by a coprecipitation method at 1200 °C. Samples with the nominal formula $(Gd_{1-x}Ca_x)(Fe_{0.95}Zn_{0.05})O_{2.975-x/2}$ (x = 0.00, 0.05, 0.10) showed single-phase orthorhombic perovskite. The presence of dopants played an important role in the reduction of Fe^{3+} to Fe^{2+} and caused different local distortions in the structure which explained the final black colouration of these pigments in comparison with the red $GdFeO_3$ sample. The loss of symmetry and the increase in the number of *d-d* transitions of iron may explain the aforementioned changes. Co-doped pigments reached low C^* values, improving on the purest black colour obtained in a commercial black ceramic pigment, which contains toxic elements. In addition to presenting good NIR solar reflectance values of up to 8%, the final colours of these pigments were also stable after their application in a commercial transparent glaze at 1080 °C that could be used for tiles.

1. Introduction

In the ceramic industry, inorganic pigments are of the utmost importance since they are the raw materials needed for colouring glazes and inks. Particularly, black pigments are extensively used and represent about 25 wt% of the total consumption [1]. Traditionally, the commercial black pigments used in the ceramic industry have been compounds with a spinel chromite/ferrite structure, mainly $CuCr_2O_4$ [DCMA 13-38-9], $(Fe,Co)Fe_2O_4$ [DCMA 13-39-9], $(Fe,Co)(Fe,Cr)_2O_4$ [DCMA 13-40-9], $(Fe,Mn)(Fe,Mn)_2O_4$ [DCMA 13-41-9] and $(Ni,Fe)(Fe,Cr)_2O_4$ [DCMA 13-50-9] due to their great stability [2,3]. Despite the fact that the aforementioned inorganic pigments contain transition elements such as nickel, cobalt, chromium and manganese, which are potentially toxic and a matter of concern to human health, they are still being used at present [4,5]. Although small amounts of these toxic elements are essential for life, their regular use is considered dangerous: cobalt is harmful to the environment [6], manganese can affect target organs [7] and chromium and nickel are carcinogens [8,9].

Fortunately, as nowadays nations around the world are aware of the need for climate protection, developed countries have taken an active stance towards approving regulations limiting the use of toxic elements in order to protect human health and the environment. As a result, over the last few years, other elements like lanthanides have become alternatives to eliminate potentially toxic elements in ceramic pigments [10–12]. Consequently, studies mainly aimed at decreasing the toxicity of ceramic black pigments and improving their optical properties have also been conducted in the present century. Researchers obtained new black inorganic pigments and improved the final colour by introducing minor variations in the traditional compositions [13–15]. Nonetheless, although in recent years studies have been carried out to obtain sustainable black pigments, the use of toxic elements has not been totally eliminated. $NiFe_{2-x}Cr_xO_4$ (x = 0.0–2.0) compositions were synthesised at 1200 °C to decrease the chrome concentration of $(Ni,Fe)(Fe,Cr)_2O_4$, and Ni^{2+} was also replaced by Mg^{2+} and Zn^{2+} [3]. $La_{1-x}Ca_xCoO_3$ black pigments (x = 0–0.4) were obtained at 800 °C by Melo et al. [16]. Additionally, Ca_2MnO_4, also with black colouration and fired at 1200 °C, presented a NIR reflectance, R_{NIR}, = 50% [17], and pigments based on $Ca_2Mn_{0.85-x}Ti_{0.15}Zn_xO_{4-x}$ (with $0 \leq x \leq 0.10$) were developed to improve the final colour without decreasing the NIR reflectance [18]. Co^{2+} doped $ZnFe_2O_4$ pigments fired at 1000 °C were also prepared and

* Corresponding author.
** Corresponding author.
E-mail addresses: fortunom@uji.es (M. Fortuño-Morte), pserna@uji.es (P. Serna-Gallén), mir@uji.es (H. Beltrán-Mir), cordonci@uji.es (E. Cordoncillo).

https://doi.org/10.1016/j.ceramint.2022.04.111
Received 9 February 2022; Received in revised form 6 April 2022; Accepted 11 April 2022
Available online 14 April 2022

Table 1
Compositions prepared based on Ca and/or Zn doped $GdFeO_3$ and their tolerance factor *t*.

Samples	General formula	*x*	*y*	Nominal Composition	Reference	*t*
Undoped $GdFeO_3$	$GdFeO_3$	0	0	$GdFeO_3$	GF	0.923
Ca-doped $GdFeO_3$	$(Gd_{1-x}Ca_x)FeO_{3-x/2}$	0.02	0	$(Gd_{0.98}Ca_{0.02})FeO_{2.99}$	C2A	0.924
		0.05		$(Gd_{0.95}Ca_{0.05})FeO_{2.975}$	C5A	0.924
	$Gd(Fe_{1-y}Ca_y)O_{3-y/2}$	0	0.05	$Gd(Fe_{0.95}Ca_{0.05})O_{2.975}$	C5B	0.915
Zn-doped $GdFeO_3$	$(Gd_{1-x}Zn_x)FeO_{3-x/2}$	0.05	0	$(Gd_{0.95}Zn_{0.05})FeO_{2.975}$	Z5A	0.920
	$Gd(Fe_{1-y}Zn_y)O_{3-y/2}$	0	0.05	$Gd(Fe_{0.95}Zn_{0.05})O_{2.975}$	Z5B	0.921
			0.10	$Gd(Fe_{0.90}Zn_{0.10})O_{2.95}$	Z10B	0.918
Ca,Zn-co-doped $GdFeO_3$	$(Gd_{1-x}Ca_x)(Fe_{1-y}Zn_y)O_{3-x/2-y/2}$	0.05	0.05	$(Gd_{0.95}Ca_{0.05})(Fe_{0.95}Zn_{0.05})O_{2.95}$	C5AZ5B	0.922
		0.10		$(Gd_{0.90}Ca_{0.10})(Fe_{0.95}Zn_{0.05})O_{2.925}$	C10AZ5B	0.923
		0.15		$(Gd_{0.85}Ca_{0.15})(Fe_{0.95}Zn_{0.05})O_{2.90}$	C15AZ5B	0.925
		0.20		$(Gd_{0.80}Ca_{0.20})(Fe_{0.95}Zn_{0.05})O_{2.875}$	C20AZ5B	0.926

the best optical results were obtained for the pigment with a 16.7 wt% of Co_3O_4 [19]. Recently, a black pigment with a perovskite structure containing at least an alkaline earth metal element, titanium, and manganese was patented in 2020 [20] and, finally, black pigments based on Cr-doped Fe_2O_3 ($C^* = 0.7$ and $R_{NIR} = 23\%$), $YMnO_3$, $Sr_4CuMn_2O_9$ ($C^* = 9.6$ and $R_{NIR} = 51\%$) and $Sr_2(Mg_{0.5}Mn_{0.5})Ge_2O_7$ were also synthesised [21].

At the same time, there are recent studies where black pigments were developed from waste containing cobalt, manganese, chromium and/or nickel [22–26]. Nevertheless, industrial waste is reprocessed and toxic elements are also employed, a fact that is detrimental to human health. Thus, we must emphasise that, as far as we are aware, there are no environment-friendly black ceramic pigments available at the moment.

For this work, amongst all the inorganic structures where iron and lanthanides are easily incorporated, perovskite-type oxides (ABO_3) with the *Pbnm* space group have been selected in order to develop a new environment-friendly black inorganic pigment. In these compounds, *A* and *B* are cations of different sizes, *A* (with a coordination number, CN, of 12) being larger than *B* (with a CN of 6). As a result, lanthanides and iron can be incorporated into *A* and *B* positions, respectively. In a recent study [12], we developed environment-friendly reddish pigments, with high near-infrared (NIR) reflectance, based on $AFeO_3$ (*A* = La, Pr, Nd, Sm, Gd, Tb, Y or Yb) synthesised by a coprecipitation method at 1200 °C. In particular, glazes pigmented with $GdFeO_3$, $TbFeO_3$ and $YFeO_3$ powders possessed the most intense reddish colouration and these powders also presented the highest NIR solar reflectance, reaching values of 50%, which makes them optimal candidates for application as cool reddish pigments in paint.

As per the above considerations, in this study we present novel ceramic black pigments that have been synthesised based on Zn^{2+} and Ca^{2+} doped $GdFeO_3$ by a coprecipitation method and fired at 1200 °C. In order to develop sustainable black pigments with a high degree of purity, the incorporation of Ca^{2+} and Zn^{2+} into the $GdFeO_3$ perovskite was chosen because these dopants are non-toxic and non-chromophore ions, present similar ionic radii to gadolinium and iron ions, the ions that conform $GdFeO_3$ perovskite, and they also have a single oxidation state, which is useful to limit the factors that may affect the colour change from red to black. Moreover, the optical properties, the chemical stability and the application of the final black powders in glaze have been studied. The results highlight the potential use of these new black pigments for high temperature applications in the ceramic industry with good reflectance. We must note that our study presents a pioneering strategy that fits together well with the stance towards the development of environment-friendly compounds and it also greatly minimises the safety hazards since the black ceramic pigments reported herein are completely free of any toxic elements.

2. Experimental section

The coprecipitation method was employed to prepare the different compositions of pigments based on Ca^{2+} and/or Zn^{2+} doped $GdFeO_3$. In particular, the synthesis methodology is the same as the one employed in a recent study where reddish perovskites with the general formula $AFeO_3$ (*A* = La, Pr, Nd, Sm, Gd, Tb, Y or Yb) were obtained [12]. The synthesised compositions with their corresponding references are labelled in Table 1. The reference of the undoped sample was formed by the initials of the metals that conform the $GdFeO_3$ perovskite, and the other references were formed by the initials of the cations that doped $GdFeO_3$, that is *C* for Ca^{2+} and/or *Z* for Zn^{2+}, with their proportion and the initial *A* or *B*, which indicate the position where they were incorporated.

In order to prepare them all, $Gd(NO_3)_3{\cdot}6H_2O$ (99.9%, Sigma-Aldrich), $Fe(NO_3)_3{\cdot}9H_2O$ (98%, Sigma-Aldrich), $Ca(NO_3)_2{\cdot}4H_2O$ (99%, Strem Chemicals) and $Zn(NO_3)_2{\cdot}6H_2O$ (98%, Labkem) were used as precursors. Besides, absolute ethanol (99.9%, Scharlab) was used as the solvent and reagent-grade ammonia solution (32%, Scharlab) was used as the precipitation agent. A general scheme of the method by which the pigments were obtained is shown in Fig. S1 of the Supplementary Information (SI). The final powders were fired at a maximum temperature of 1200 °C for 12 h in an air atmosphere, using a heating rate of 5 °C/min. Besides, to assess the application of the final products in glazes, the pigments were mixed with a transparent commercial frit (4 wt% of the pigment), the composition of which is shown in Table S1 of the SI, and the pigment-frit mixtures were fired at a maximum temperature of 1080 °C (more detailed information about the procedure followed for the preparation of the coloured glazes can also be found in the SI).

The characterisation techniques used to study the structural and optical properties of the synthesised pigments were: X-ray diffraction (XRD), energy dispersive X-ray spectrometry (EDX), Raman spectrometry, X-ray photoelectron spectroscopy (XPS), UV–Vis–NIR spectroscopy, and simultaneous thermogravimetric and differential scanning calorimetry (TG-DSC) was used to determine the thermal stability of the pigments. Moreover, the chemical stability of the pigments was studied by the same method used in the work [12] but in this case the stirring times employed were 30 min and 24 h. Detailed information about the different characterisation equipment used and the thermal and chemical stability can be found in the SI.

3. Results and discussion

3.1. Structural and chemical properties of the powdered pigments

Before performing the structural characterisation, the Goldschmidt tolerance factor *t* can also shed some light on the stability and the distortion of the crystal structure. For orthoferrites doped at *A*/*B* sites with the general formula $(A_{1-x}A'_x)(B_{1-y}B'_y)O_{3-\delta}$, the tolerance factor was calculated using equation (1):

$$t = \frac{(1-x)R_A + xR_{A'} + R_O}{\sqrt{2}[(1-y)R_B + yR_{B'} + R_O]} \quad (1)$$

Table 2
Ionic radii of the different species occupying positions *A* (CN = 12) or *B* (CN = 6) in perovskites with the general formula ABO_3. It has been considered that Fe cations are in a high-spin state.

Specie	Position *A* (Å)	Position *B* (Å)
Gd^{3+}	1.27	0.938
Fe^{2+}	1.13	0.78
Fe^{3+}	0.99	0.645
Ca^{2+}	1.34	1.00
Zn^{2+}	1.11	0.74

where R_i are the corresponding ionic radii of the different ions [27]. For an ideal cubic perovskite, t is close to 1, otherwise it has a distorted structure, such as orthorhombic, rhombohedral or tetragonal [28].

In order to determine the values of t, it is necessary to know the ionic radii of the different cations involved in this study. The ionic radii of some cations with different coordination number (CN), especially those with CN > 8, are not included in Shannon's data [29]. Notwithstanding, the ionic radii for a certain CN can be determined according to equation (2):

$$R_N = R_{N-1} + \left(\frac{0.00135}{N-1}\right)^{1/3} \quad (2)$$

where R_N and R_{N-1} are the ionic radius of an ion with coordination numbers N and $(N-1)$, respectively [30]. For the particular case of a CN = 12 (species occupying positions *A* in the orthoferrite) and using the value of R_8 (available in the database), the above expression results in the next one (equation (3)):

$$R_{12} = R_8 + \sum_{i=8}^{11}\left(\frac{0.00135}{i}\right)^{1/3} \quad (3)$$

Table 2 presents the ionic radii of the different species involved in the crystal structure. Regardless of the postulated nominal formula, it should also be noted that dopants might occupy positions *A*/*B* interchangeably throughout the small segregation of a secondary phase, which would be rich in Gd/Fe depending on the mechanism of substitution.

Hence, as can be seen in Table 1, similar tolerance factors around 0.92 were obtained for all the compositions prepared, thereby suggesting that there was no substantial distortion of the host lattice in comparison to the undoped compound ($GdFeO_3$). In all cases, t was below, but very close to, unity and this means that *A* ions were smaller than the dodecahedral interstices. Thus, the FeO_6 octahedra tilt and rotate leading to closer packing with an orthorhombic structure *Pbnm* [31]. Notwithstanding, it is important to mention that these results refer to the theoretical nominal formulas proposed in Table 1.

The XRD patterns of the final powders fired at 1200 °C were obtained and are shown in Fig. 1. The characteristic peaks of the orthorhombic $GdFeO_3$ perovskite with the *Pbnm* space group [JCPDS-ICDD 47–67] were identified in all the synthesised compositions. In spite of this, some of the doped samples showed small peaks corresponding to secondary phases.

In detail, when $GdFeO_3$ perovskite was doped with calcium in *A* or *B* positions, the XRD patterns (Fig. 1a) showed a secondary phase attributed to $Gd_3Fe_5O_{12}$ [JCPDS-ICDD 48–77] or Gd_2O_3 [JCPDS-ICDD 12–797], respectively. With respect to the Zn-doped $GdFeO_3$ samples (Fig. 1b), when zinc was incorporated in *A* position with $x = 0.05$ (Z5A), a secondary phase related to $Gd_3Fe_5O_{12}$ [JCPDS-ICDD 48–77] was obtained. On the other hand, when zinc was added to the *B* position with $y = 0.05$ (Z5B), no secondary phase was identified, but when its concentration was increased until $y = 0.10$ (Z10B), a small peak corresponding to Gd_2O_3 [JCPDS-ICDD 12–797] was found. Thus, the only sample doped with one cation that presented a unique phase is Z5B.

Nonetheless, when both cations were present, Ca^{2+} at site *A* and Zn^{2+}

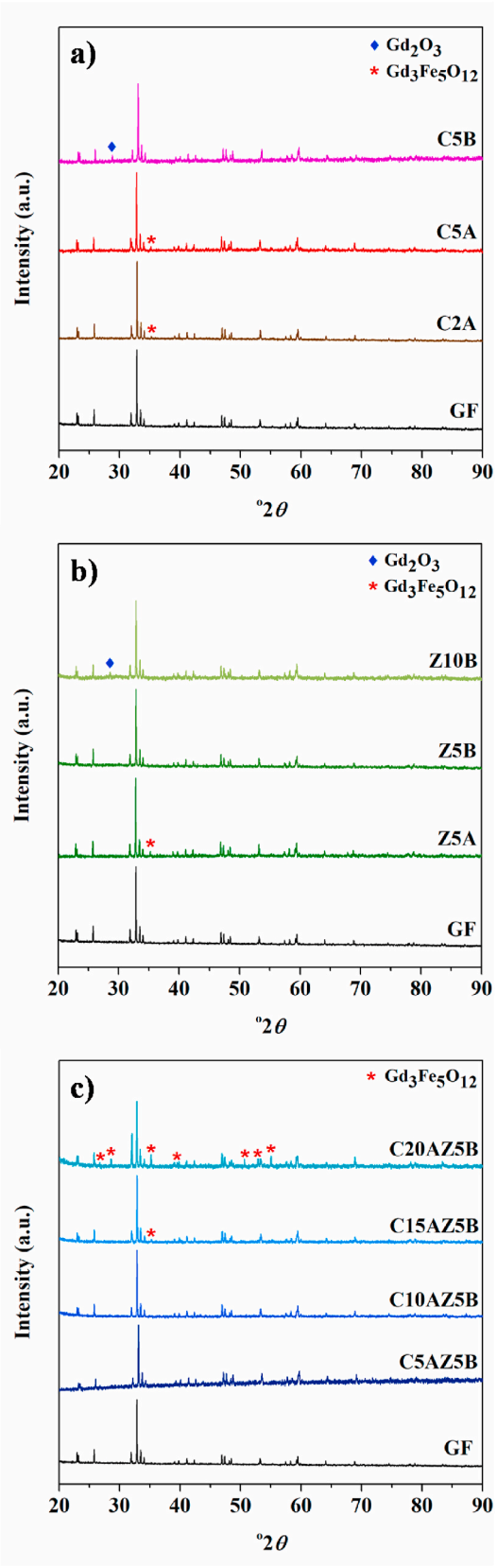

Fig. 1. XRD patterns for powder samples fired at 1200 °C for 12 h: (a) Ca-doped $GdFeO_3$, (b) Zn-doped $GdFeO_3$, and (c) Ca, Zn-co-doped $GdFeO_3$. The XRD pattern for undoped $GdFeO_3$ is included in all figures for comparison.

Table 3
χ^2 values of the refinements and refined unit cell parameters of the powders. Space Group = 62 (*Pbnm*).

Powder	χ^2	*a* (Å)	*b* (Å)	*c* (Å)	*V* (Å^3)
GF	1.38	5.3529	5.6120	7.6734	230.52
Z5B	1.30	5.3509	5.6120	7.6688	230.29
C5AZ5B	1.21	5.3462	5.6008	7.6592	229.34
C10AZ5B	1.28	5.3515	5.5987	7.6654	229.68

at site *B* (Fig. 1c), the secondary phase attributed to $Gd_3Fe_5O_{12}$ [JCPDS-ICDD 48–77] was only formed for samples with the highest Ca^{2+} concentration ($x = 0.15$ and 0.20). Thus, the presence of zinc in the structure facilitated the incorporation of calcium into the perovskite, probably due to distortions in the lattice.

From now on, the results will be focused only on the GF sample and doped and co-doped compositions that exhibited a single-phase (Z5B, C5AZ5B and C10AZ5B). In addition, the XRD patterns of these compositions were refined and the results are presented in Fig. S2 of the SI and Table 3. The goodness of fit parameter χ^2 (Table 3) showed that the refinements were correct and the orthorhombic perovskite phase with the *Pbnm* space group was observed in all the samples with a single-phase. Furthermore, as can be seen in Table 3, the unit cell volume decreased for doped and co-doped perovskites.

In order to study the morphology and size of the particles of single-phase samples, SEM was implemented. Fig. 2 presents the SEM images of GF, Z5B and C5AZ5B fired at 1200 °C. The SEM image of GF (Fig. 2a) revealed a uniform particle size distribution slightly smaller than 1 μm and particles with straight boundaries. Otherwise, particles of the doped samples, shown in Fig. 2b and c, presented a higher degree of sintering in comparison to the undoped samples. Moreover, the EDX results of the four single-phase samples confirmed that there was no presence of secondary phases in any of them and each powder presented similar atomic proportions in different areas studied. In addition, their stoichiometric ratios are in accordance with their general formula, shown in Table S2 of the SI, which presents the average content of the elements from the EDX analysis at 25 different points considered to be representative of each sample. Furthermore, an EDX spectrum with the corresponding region for C5AZ5B ratios is illustrated in Fig. S3 of the SI as an example.

So as to study the possible local distortions caused in the structure due to the doping of $GdFeO_3$ with Zn^{2+} and Ca^{2+}, Raman spectra at room temperature in the 90–700 cm^{-1} range were reported. Before examining the different Raman spectra obtained for each sample, it is essential to note that compounds synthesised in this study crystallised in the *Pbnm* space group that gives rise to 24 Raman-active vibrational modes, which can be represented with Mulliken symbols as $\Gamma = 7\,A_g \oplus 7\,B_{1g} \oplus 5\,B_{2g} \oplus 5\,B_{3g}$ [32]. In accordance with the literature [33–35], the wavenumber modes below 200 cm^{-1} are essentially associated to displacements of ions in position *A*, because of vibrations of *A* and O, specifically *A*–O stretching vibrations. Raman peaks in the region between 200 cm^{-1} and 350 cm^{-1} are attributed to BO_6 octahedral tilting. In addition, active bands from 350 cm^{-1} to 500 cm^{-1} are related to out-of-phase oxygen bending motions, specifically, oxygen octahedral bending vibrations. Lastly, symmetric *B*–O stretching vibrations are above 500 cm^{-1}.

The Raman spectra of GF, Z5B and C5AZ5B compositions are shown in Fig. 3 (the Raman spectrum of C10AZ5B is analogous to that of the co-doped C5AZ5B sample). As can be shown in this figure, the sums of the Lorentzian functions were used to perform the spectra deconvolution and make it possible to know the position of all the Raman-active modes; the peak positions of each sample studied that were consistent with the reported literature [35,36] are listed in Table S3 of the SI. Not all the expected modes were identified because some of them were probably either masked by band overlap or their intensity was below the detection limit.

The Raman spectrum of the undoped sample (Fig. 3a) offered weak changes with respect to the doped samples (Fig. 3b and c). Nevertheless, there are peaks marked with an arrow symbol that are only present in doped samples, probably because of the local distortions caused by the dopants that have different ionic radii to the cations that conform the undoped perovskite [37] (see Table 2). First, the peak around 170 cm^{-1} is only found in co-doped samples. This can be explained by the fact that Raman modes below 200 cm^{-1} are related to doping at site *A* [38], namely in samples where Ca^{2+} is doping the Gd^{3+} site. On the other hand, the peaks around 200 and 595 cm^{-1} are in the three doped samples. The addition of dopants to the $GdFeO_3$ perovskite originated oxygen vacancies and could modify the Fe–O stretching vibrations inside octahedral units because of distortions introduced by vacancies [35]. Hence, a change in the symmetry was reflected in the identification of more Raman-active modes with an increase in the doping. As a consequence of the local distortion in the structure caused by doping, an important modification could be achieved in the final colour of the powders that were synthesised.

It is also important to emphasise that according to the nominal formula, all compositions, except the GF sample, are oxygen-deficient. Therefore, it might be possible that partial reduction of Fe^{3+} to Fe^{2+} occurs in the host lattice in favour of the generation of oxygen vacancies through O_2 release (equations (4)–(6)):

$$2\left[Fe^{3+}(s) + 1\ e^- \leftrightarrow\ Fe^{2+}(s)\right] \quad (4)$$

$$O^{2-}(s) \leftrightarrow {}^1\!/\!_2 O_2(g) + 2e^- \quad (5)$$

$$2Fe^{3+}(s) + O^{2-}(s) \leftrightarrow 2Fe^{2+}(s) + {}^1\!/\!_2 O_2(g) \quad (6)$$

XPS spectra of Fe 2*p* and Fe 3*p* for the four single-phase samples were obtained to confirm this oxidation-reduction mechanism. Deconvolution of the spectra was performed by mixed Gaussian-Lorentzian fit (60:40). Similar XPS spectra of Fe 2*p* for the four samples are shown in Fig. 4a and the deconvolution of Fe 2*p* for C10AZ5B is presented in Fig. 4b as an example. According to the literature [39], the binding energies (BE) of Fe_2SiO_4 (Fe^{2+}) and Fe_2O_3 (Fe^{3+}) for the Fe $2p_{3/2}$ core level peaks are 709.0 eV and 711.0 eV, respectively, the associated satellites were found at 714.7 and 718.8 eV, and as regards Fe $2p_{1/2}$, the BE of Fe_2SiO_4 (Fe^{2+}) and Fe_2O_3 (Fe^{3+}) are found at 722.6 eV and 724.4 eV, respectively. Hence, in all cases, the characteristic BE of Fe^{2+} and Fe^{3+} for Fe $2p_{1/2}$, Fe

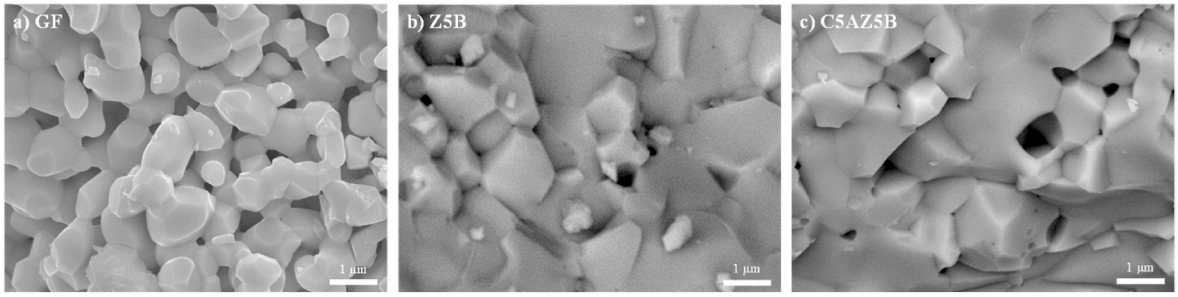

Fig. 2. SEM images of the powders fired at 1200 °C: (a) GF, (b) Z5B, and (c) C5AZ5B.

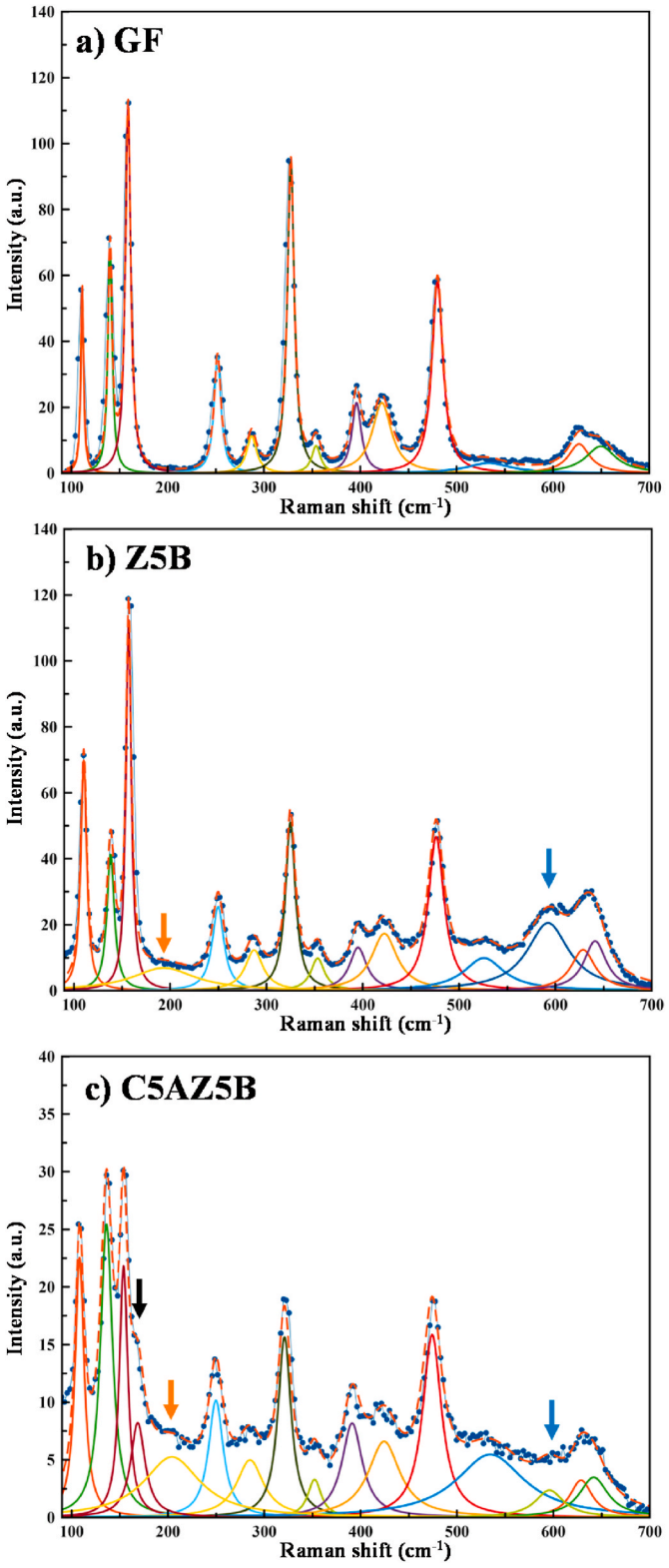

Fig. 3. Raman spectra deconvolution of the powders fired at 1200 °C: (a) GF, (b) Z5B, and (c) C5AZ5B.

$2p_{3/2}$ and their satellites were identified in the XPS spectra.

As carried out in recent studies [40], in order to quantify the amount of Fe^{2+} and Fe^{3+} in each sample, the area of the Fe $2p_{3/2}$ peaks of both cations were determined. As shown in Fig. 4c–f, the maximum intensity of the Fe $2p_{3/2}$ peak is essentially the same for the four samples studied but as doping increased, the content of divalent iron ions rose from 9% to 24%, which indicates that the presence of zinc and calcium facilitate the partial reduction of Fe^{3+} to Fe^{2+} and, as a consequence, co-doped samples present a higher Fe^{2+} content.

In the same way, the Fe 3*p* spectra confirm the above-mentioned tendency of the amount of Fe^{2+} and Fe^{3+} in the samples. Each XPS spectrum of Fe 3*p* for the four samples and their deconvolution are presented in Fig. S4 of the SI. Bearing in mind the literature [39,41,42], all Fe 3*p* spectra consist of both Fe $3p_{1/2}$ and Fe $3p_{3/2}$, but a single broad peak with no separation between $3p_{1/2}$ and Fe $3p_{3/2}$ lines was obtained because the spin-orbit splitting between the two photoelectron peaks is very small. After the deconvolution of the 3*p* peak into two peaks, the lower BE transition is attributed to Fe^{2+} ions and the higher BE transition is attributed to Fe^{3+} ions. Accordingly, as the maximum intensity of the 3*p* peak shifted to lower energies when the amount of dopants increases, the amount of Fe^{2+} was greater in the doped samples.

As a result of XPS studies, iron was present in both oxidation states (Fe^{2+} and Fe^{3+}) in the four final powders. In addition, as the amount of dopants increases, a greater amount of Fe^{2+} is expected to be found in the doped samples because the maximum intensity of the main bands shifts to lower energies.

3.2. *Optical and colorimetric properties of the powdered pigments*

Once the structural characterisation was completed and the tendency of the oxidation states on iron in the samples was determined, UV–Vis spectroscopy was performed in order to study their optical properties. The UV–Vis reflectance of the four fired powders that present a single-phase in the 300–750 nm range are shown in Fig. 5 and the colour difference between GF and the other three powders is confirmed. The undoped sample spectrum exhibited an intense band centred at ≈ 600 nm that confirmed the red colouration of this powder. Moreover, the spectra of the doped samples showed low reflectance in all the UV–Vis range studied, thus verifying the black colouration of these compositions.

Fig. 6 shows the absorbance spectra of the different samples and, the GF spectrum also offered important differences in comparison to the others. In the spectrum of the GF compound, a broad and strong band associated with the $O_{2p} \rightarrow Fe_{3d}$ charge transfer transitions and the *d-d* transitions of Fe^{3+} was observed from 350 to 550 nm [43]. The deconvolution of this spectrum is presented in Fig. 6a, where the band obtained at 355 nm is associated with $O_{2p} \rightarrow Fe_{3d}$ charge transfer transitions and the other four broad bands are in agreement with *d-d* transitions of Fe^{3+} ions: 404 nm ($^6A_1 \rightarrow {}^4E$, $^4T_2$ transition), 466 nm ($^6A_1 \rightarrow {}^4E$, ^4A transition), 530 nm ($^6A_1 \rightarrow {}^4T_2$ transition) and 697 nm ($^6A_1 \rightarrow {}^4T_1$ transition) [43]. However, the sharp absorptions associated with Gd^{3+} are very weak because the *f-f* transitions are forbidden by Laporte's parity selection rule and, besides, this cation can only absorb UV radiation with wavelengths smaller than 311 nm [44]. However, the black samples (Fig. 6b) presented a high absorbance in all the UV–Vis range, and it was thus difficult to determine the different associated transitions. This fact could be associated with a larger number of bands as a result of the local distortion of the structure, that is, a change in the site-symmetry [45].

Furthermore, the chromatic parameters of these powders and their final colour are shown in Fig. 7. The values of the chromatic coordinates of GF confirmed the reddish colouration of the powder. However, the other three samples with a small amount of Zn^{2+} or Zn^{2+} and Ca^{2+} presented a decrease in L^* values, which were found to be around 42 in all of them, a^* values were between −0.01 and 0.47 and b^* values were between −0.34 and 1.14. As a result, saturation (C^*) had values from −0.40 to 1.22, C5AZ5B and C10AZ5B being the samples that presented the best black colouration with the lowest C^* values. Moreover, knowing that a commercial black ceramic pigment that contains iron, nickel, cobalt, chromium and manganese that is currently in use presented a similar L^* value and a small increase in the saturation parameter (L^*, a^*, b^* and C^* are 41.98, 0.16, 0.61 and 0.65, respectively), it can be stated

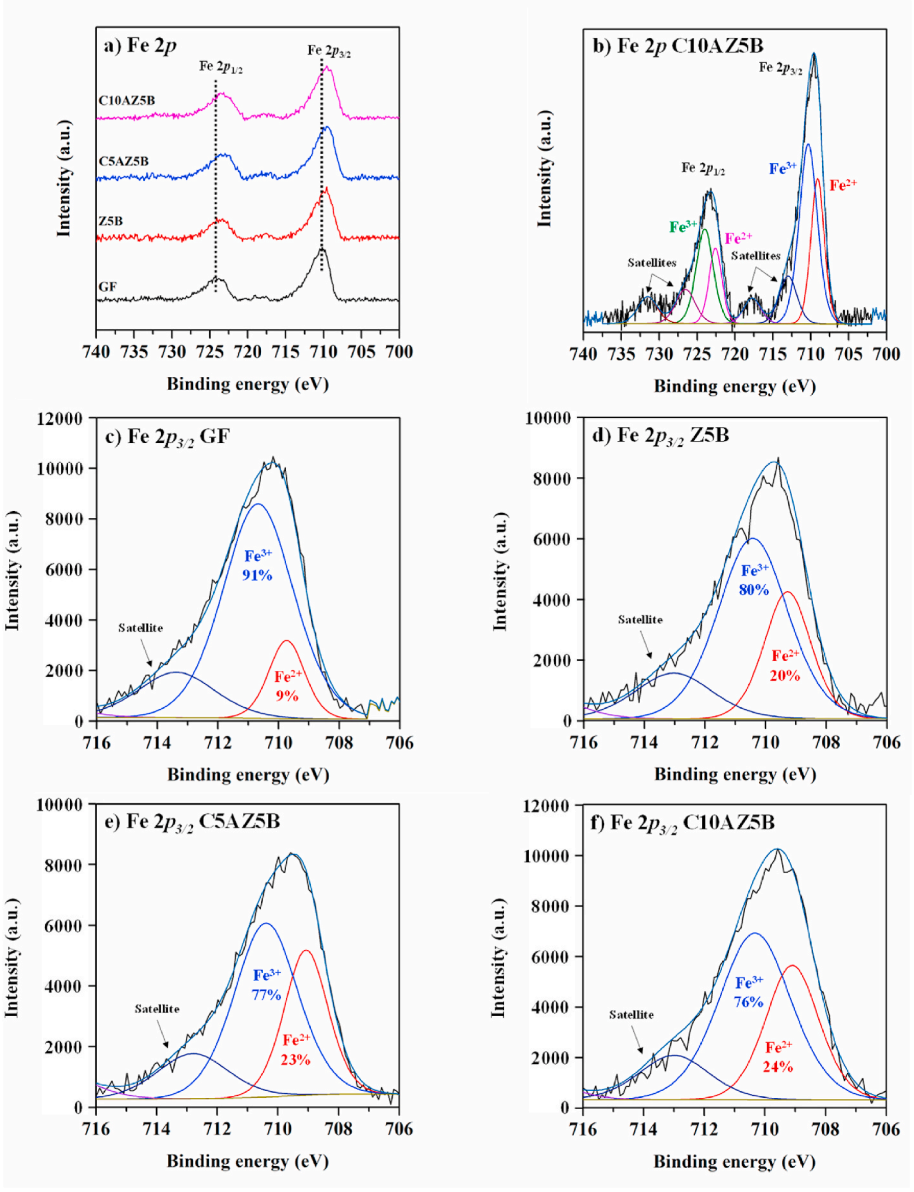

Fig. 4. (a) XPS spectra of Fe 2*p* for single-phase samples; (b) XPS spectrum deconvolution of Fe 2*p* for C10AZ5B; (c) Fe $2p_{3/2}$ peak deconvolution for GF; (d) Fe $2p_{3/2}$ peak deconvolution for Z5B; (e) Fe $2p_{3/2}$ peak deconvolution for C5AZ5B; (f) Fe $2p_{3/2}$ peak deconvolution for C10AZ5B.

that C5AZ5B and C10AZ5B compositions, free of any toxic elements, present a better pure black colouration than commercial black pigments. Above and beyond this, in C10AZ5B powders the gadolinium content decreases and so does their production cost.

Moreover, as can be seen in Fig. 8, the black pigments C10AZ5B that were prepared present a lower C^* value than the reported black powders that can be employed in high temperature applications (the C^* values for the different black pigments were obtained by the a^* and b^* parameters provided in each corresponding paper, employing equation S(2) of the SI). This fact confirms that the sustainable pigments developed in this work have an excellent black colouration with high purity, better than all the reported ones.

3.3. Evaluation of the colouring performance of the pigments in glaze

At this point, it is also important to note that the inorganic pigment synthesised at 1200 °C should be stable and exhibit a good colour when it is added to different media. Thus, a powdered pigment-frit mixture was prepared and fired according the cycle set out in the experimental section at the maximum temperature of 1080 °C. The L*, a^*, b^* and C^* chromatic coordinates of the pigmented glaze were obtained. A photograph of the compositions after their application in the frit with their corresponding coordinates is also shown in Fig. 7. The reddish colouration of the GF composition improves and, focused on the three black pigments, they also offered good stability in this media because a^* had values from 2.22 to 1.49 and b^* had values from 1.09 to 1.48. Subsequently, low values of C^*, between 1.85 and 2.68, were found, C10AZ5B being the pigment that developed the purest black colouration with the lowest values of a^*, b^* and C^*. The crystalline phase of the pigment remained after treatment of the pigment-frit mixture at 1080 °C, as can be seen in Fig. S5 of the SI, where the main peaks of the perovskite were found, together with the amorphous halo of the majority vitreous matrix for the C10AZ5B powder-frit mixture. Analogous results were obtained for the other coloured ceramic glazes. Hence, the results confirmed that the perovskite crystalline phase of the pigment remains after that treatment.

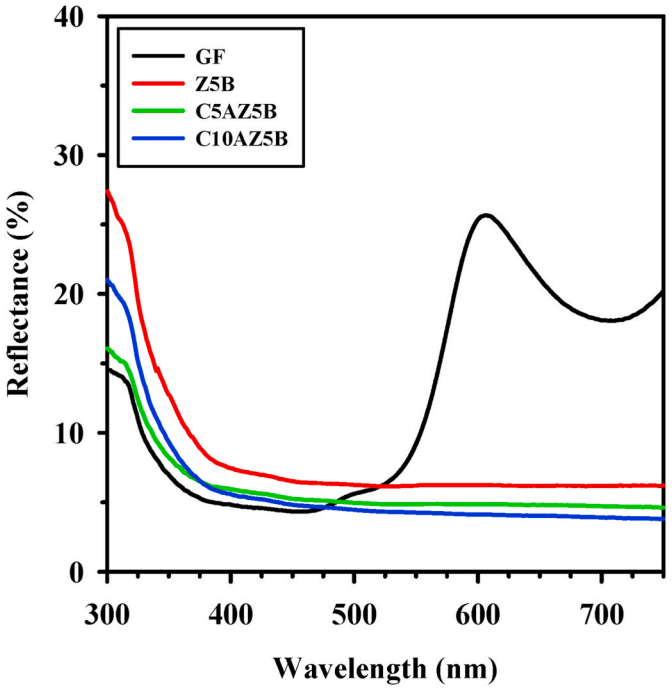

Fig. 5. UV–Vis reflectance spectra of GF, Z5B, C5AZ5B and C10AZ5B powders.

3.4. Mechanism of colour in powdered pigments

Before discussing the mechanism by which colour is produced in the powdered pigments developed in the present work, it is important to remember that the final colour of a pigment is affected by the chromophore ions present in the crystal structure. In particular, it is fundamental to consider the *d-d* transitions that take place, the oxidation state of the chromophore, and its local distortion. Regarding black powders in which iron is the only chromophore in the host lattice, as in this study, it is of particular interest to analyse the well-known magnetite (Fe_3O_4), which has an inverse cubic spinel structure (AB_2O_4) [46]. The crystal structure of this spinel consists of a unit cell with the oxygen ions in a close-packed FCC structure and iron ions forming the tetrahedral and the octahedral subunits: $[Fe^{3+}]_A[Fe^{2+}Fe^{3+}]_BO_4$, where the tetrahedral position is occupied by the Fe^{3+} ions and the octahedral position is occupied by Fe^{2+} and Fe^{3+} ions [47]. Therefore, the black colouration of the magnetite could be associated with the presence of both oxidation states of iron (Fe^{2+} and Fe^{3+}) as well as the presence of iron in both tetrahedral and octahedral positions in the crystal structure.

With the purpose of determining the factors influencing the colour transition from red to black produced between the undoped sample and the doped samples, the previous results about the oxidation state of iron (the only chromophore cation in the structure) were taken into account. In view of this, to know whether the increased population of Fe^{2+} in doped samples determines the final black colour, the C10AZ5B sample was oxidised with an oxygen atmosphere at a maximum temperature of 900 °C for 2 h with the aim of promoting the oxidation of Fe^{2+} to Fe^{3+}.

To confirm the oxidation process, the XRD of the oxidised C10AZ5B sample was compared with the original C10AZ5B sample (Fig. S6a of SI). The characteristic peaks of the orthorhombic $GdFeO_3$ perovskite with the *Pbnm* space group [JCPDS-ICDD 47–67] were also observed in the oxidised compound. Moreover, when the C10AZ5B composition was oxidised, a displacement towards higher °2θ angles of the Bragg peaks could be observed in the XRD patterns with respect to the C10AZ5B sample (see Fig. S6b of SI). This fact is understandable according to Bragg's law, $n\cdot\lambda = 2\ d\cdot\sin\theta$, where d is the interplanar distance, θ is the diffraction angle, and λ is the diffraction wavelength. Based on the radii (see Table 2), Fe^{3+} has a smaller ionic radius than Fe^{2+} [29]. Thus, if oxidation occurred, iron was found as Fe^{3+} and, as a result, the interplanar distance decreases and therefore the °2θ angle increases. Furthermore, the oxidation process of iron is examined by comparing the XPS spectra of the Fe 2*p* results before and after oxidation (Fig. S7a of SI): the maximum intensity of Fe $2p_{1/2}$ and Fe $2p_{3/2}$ peaks are moved to longer binding energies for the oxidised sample. The XPS spectrum of Fe 2*p* for the oxidised sample (Fig. S7b of SI) showed that this sample contains a higher amount of Fe^{3+} (87%) than the non-oxidised sample C10AZ5B (76%). In accordance with this, the oxidation of Fe^{2+} to Fe^{3+} took place at 900 °C, but oxidised C10AZ5B powders preserved their original black colouration. As a consequence, the partial reduction of Fe^{3+} to Fe^{2+} favoured by the addition of Ca^{2+} and Zn^{2+} is not the main factor that caused the black colouration for doped GF samples.

Considering the Raman spectroscopy results and that iron is the only chromophore cation present in the compositions, the aspect that could contribute to the major change in the colour of perovskite from red to black could be local distortions of the ions. More specifically, this refers to a change in symmetry due to the introduction of Ca^{2+} and Zn^{2+} into the initial reddish perovskite, where there is a difference between the ionic radii of the dopants and the metals that conform the initial GFO perovskite. Thus, the lack of symmetry of Fe^{2+}/Fe^{3+} sites may promote the existence of more transitions due to the relaxation of the selection rules and the existence of a different distribution of energy levels. As a consequence, UV–Vis absorbance spectra for black powdered pigments could present a larger number of bands, which would explain their colouration [43,45].

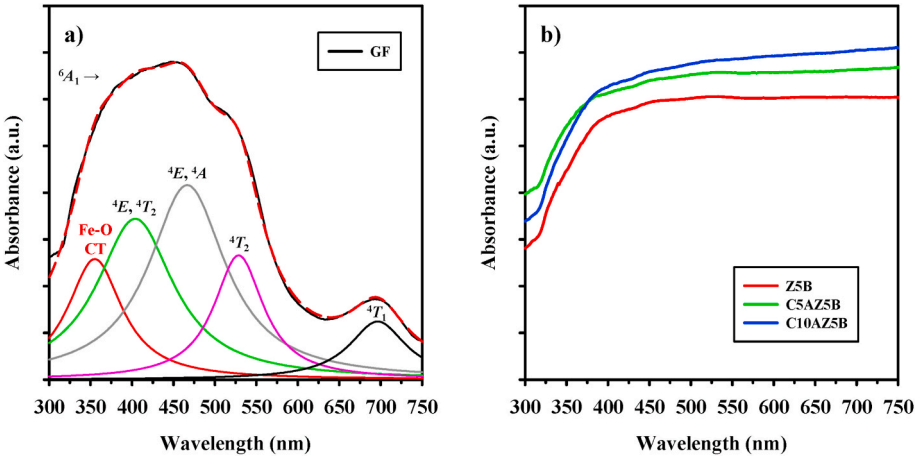

Fig. 6. Absorbance spectra of the powders fired at 1200 °C: (a) GF, (b) Z5B, C5AZ5B and C10AZ5B.

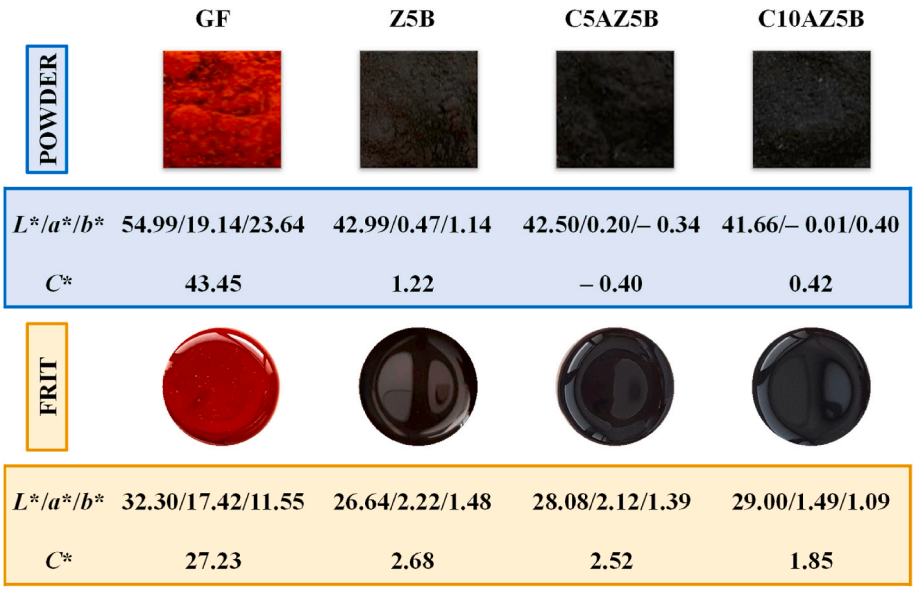

Fig. 7. Photographs of powders and pigmented glazes with their corresponding chromatic coordinate values.

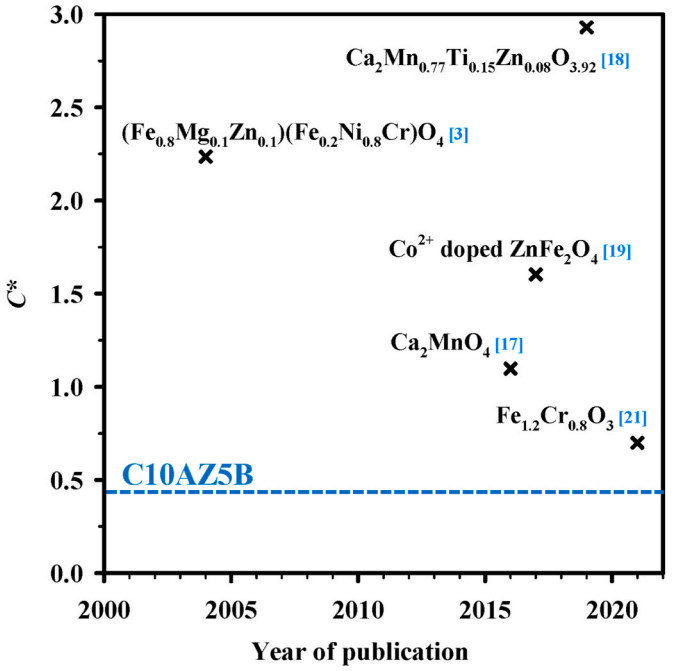

Fig. 8. C^* values of the pigment C10AZ5B that was prepared and those reported for high temperature applications. The C^* value for the C10AZ5B sample is indicated with a discontinuous line.

3.5. Studies of the thermal and chemical stability of the powdered pigments

In order to finalise the evaluation of the synthesised pigments and due to its excellent black colouration, the C10AZ5B composition was selected in order to study the thermal and chemical stability of the synthesised pigments.

Thermogravimetric analysis in the temperature range from 50 °C to 1200 °C was used to evaluate the thermal stability of C10AZ5B. Furthermore, as a reference, the GF sample was also studied. Fig. S8 of the SI presents the TG-DSC curves for these compounds and a negligible weight change and phase transition of the pigments was observed in this temperature range, which indicated that the pigments were thermally stable.

In order to determine the chemical stability of C10AZ5B powders, this sample was treated with solutions at three different pH values: acid (5 wt% HNO_3), alkali (5 wt% NaOH) and deionised water. To do this, 0.2500 g of C10AZ5B powders were soaked in the solutions for 30 min and 24 h with constant stirring using a magnetic stirrer. Following this, the different samples were filtered, washed with deionised water, dried and weighed again. The final weight, the chromatic coordinates and the total colour differences (ΔE^*) of the tested compound after the chemical stability studies for both stirring times are enumerated in Table 4. In all cases, an insignificant weight loss was detected and small differences in the chromatic coordinates of the tested sample were determined. As a result, low values of total colour differences (ΔE^*) were obtained, which indicated that the black pigment is chemically stable in the three different media tested.

3.6. Evaluation of the NIR solar reflectance

Focusing on final black powders, it is also important to evaluate their

Table 4
Final weight, chromatic coordinates and the total colour differences of the C10AZ5B pigment after treatment in the different media after 30 min and 24 h of stirring.

Test for C10AZ5B	30 min						24 h					
	pH	m_{final} (g)	L^*	a^*	b^*	ΔE^*	pH	m_{final} (g)	L^*	a^*	b^*	ΔE^*
Air	–	0.2500	41.66	−0.01	0.40	–	–	0.2500	41.66	−0.01	0.40	–
Acid	1.69	0.2472	41.67	0.00	−0.35	0.75	1.62	0.2479	41.52	0.06	0.02	0.41
Alkali	12.03	0.2468	41.59	0.01	−0.23	0.63	12.15	0.2484	41.62	0.12	−0.23	0.64
Water	6.84	0.2486	41.91	0.12	0.10	0.41	6.95	0.2467	41.55	0.64	0.50	0.67

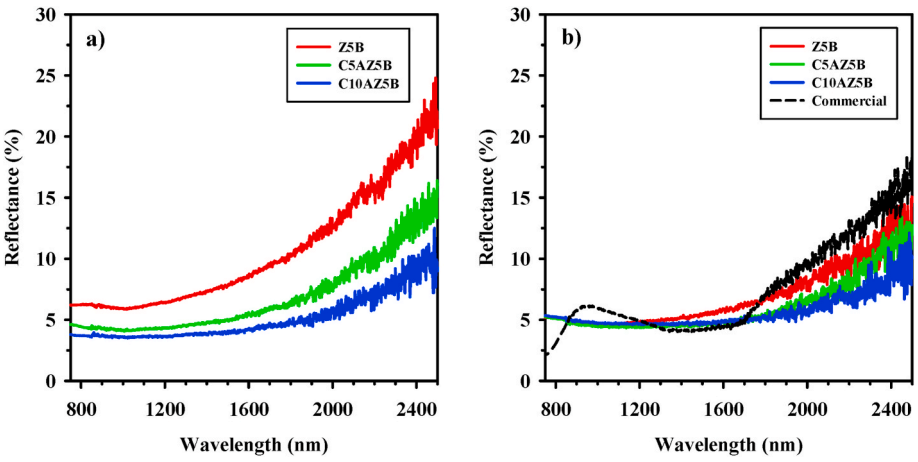

Fig. 9. (a) NIR reflectance spectra of Z5B, C5AZ5B and C10AZ5B powders; (b) NIR reflectance spectra of black pigment-frit mixtures.

reflectance. Fig. 9a shows their NIR reflectance spectra. The black final powders showed very similar spectra with the highest NIR reflectance ≈25%. The NIR solar reflectance values of the pigments took the values of 8%, 5% and 4% for Z5B, C5AZ5B and C10AZ5B, respectively. Besides, the three black ceramic pigments synthesised offered total solar reflectance (R_T) values of 7% for Z5B, 5% for C5AZ5B and 5% for C10AZ5B, similar R_T values to conventionally black pigments like carbon black that present a total solar reflectance of 6% [1].

Moreover, Fig. 9b depicts the NIR reflectance spectra of these three samples and of the black commercial pigment used as a reference with their application in the same frit. In all cases, NIR reflectance acquired similar representation with values between 2.5 and 15% over all the range, and more specifically the NIR solar reflectance values were 5% for all the black glazes obtained. In addition, the black glaze prepared with the commercial black pigment presented the same NIR solar reflectance value of 5%. As a consequence, new environment-friendly black ceramic pigments with good optical properties have been synthesised in this study.

To sum up, environment-friendly black pigments based on Ca^{2+} and Zn^{2+} doped $GdFeO_3$ with good solar reflectance were synthesised in the present work for high temperature applications to be used, in particular, as pigments for ceramic glazes. C10AZ5B is the pigment that presented the purest black colouration.

4. Conclusions

Novel environment-friendly black pigments based on Ca^{2+} and Zn^{2+} doped $GdFeO_3$ were prepared by the coprecipitation method at 1200 °C. The $GdFeO_3$ orthorhombic perovskite that crystallised in the *Pbnm* space group was obtained in $GdFeO_3$ and $(Gd_{1-x}Ca_x)(Fe_{0.95}Zn_{0.05})O_{2.975-x/2}$ (x = 0.00, 0.05, 0.10) compositions without any secondary phase. Doped samples presented a higher degree of sintering than the $GdFeO_3$ composition. Moreover, Raman spectroscopy confirmed that the oxygen vacancies, generated by the incorporation of Ca^{2+} and Zn^{2+} into the $GdFeO_3$, produced a distortion on the Fe–O stretching vibrations inside FeO_6 octahedral units and, as shown by the results of the XPS, the dopants also promoted the partial reduction of Fe^{3+} to Fe^{2+}. These facts could be associated with the important red-to-black colour change experienced from undoped to doped $GdFeO_3$ compositions.

Focusing on the three black pigments, which have a^* and b^* values close to zero, their saturation (C^*) values were achieved from −0.40 to 1.22, C5AZ5B and C10AZ5B being the samples that present the purest black powder colouration with C^* values of −0.40 and 0.42, respectively. Furthermore, the two pigments mentioned above improved the colouration of a currently commercial black ceramic pigment that contains toxic elements with a C^* value of 0.65. The pigments also exhibited a good stability when they were applied to a transparent commercial frit at 1080 °C, with C10AZ5B as the composition that presented the lowest a^*, b^* and C^* values. With respect to the NIR solar reflectance, the three black powders studied offered values of 8%, 5% and 4% for Z5B, C5AZ5B and C10AZ5B, respectively, and a NIR solar reflectance of 5% was obtained for all black glazes, that is, for synthesised commercial pigments. Moreover, the final powders also had good thermal and chemical stability.

Consequently, novel sustainable black ceramic pigments with high purity based on Ca^{2+} and Zn^{2+} doped $GdFeO_3$ with good NIR solar reflectance synthesised in this study are optimal for high temperature applications like glazes for tiles. In our view, these are the black ceramic pigments with the best purity without any toxic elements developed to date.

Declaration of competing interest

The authors declare that they have no known competing financial interests or personal relationships that could have appeared to influence the work reported in this paper.

Acknowledgments

This work was financially supported by the Spanish Ministerio de Ciencia e Innovación [Project PID2020-116149 GB-I00] and the Universitat Jaume I [UJI-B2019-41]. P. Serna-Gallén also thanks the Spanish Ministerio de Ciencia, Innovación y Universidades for an FPU predoctoral contract.

Appendix A. Supplementary data

Supplementary data to this article can be found online at https://doi.org/10.1016/j.ceramint.2022.04.111.

References

[1] S. Jose, D. Joshy, S.B. Narendranath, P. Periyat, Recent advances in infrared reflective inorganic pigments, Sol. Energy Mater. Sol. Cell. 194 (2019) 7–27, https://doi.org/10.1016/j.solmat.2019.01.037.

[2] DCMA, Classification and Chemical Description of the Mixed Metal Oxide Inorganic Coloured Pigments, second ed., Dry Color Manufacturers' Association, Arlington, Va, 1982. Metal Oxides and Ceramic Colors Subcommittee.

[3] J. Calbo, S. Sorlí, M. Llusar, M.A. Tena, G. Monrós, Minimisation of toxicity in nickel ferrite black pigment, Br. Ceram. Trans. 103 (2004) 3–9, https://doi.org/10.1179/096797804225012729.

[4] D.R. Swiler, E.A. Axtell, Rare Earth Manganese Oxide Pigments, 2003.

[5] P.H. Holgado, M.J. Holgado, M.S. San Román, V. Rives, Ni-Fe mixed oxides prepared by calcination of layered double hydroxides: potential pigments for the ceramic industry, Ceram. Int. 41 (2015) 8451–8460, https://doi.org/10.1016/j.ceramint.2015.03.047.

[6] N. Pandey, C.P. Sharma, Effect of heavy metals Co^{2+}, Ni^{2+} and Cd^{2+} on growth and metabolism of cabbage, Plant Sci. 163 (2002) 753–758, https://doi.org/10.1016/S0168-9452(02)00210-8.

[7] P. Huang, G. Li, C. Chen, H. Wang, Y. Han, S. Zhang, Y. Xiao, M. Zhang, N. Liu, J. Chu, L. Zhang, Z. Sun, Differential toxicity of Mn^{2+} and Mn^{3+} to rat liver tissues: oxidative damage, membrane fluidity and histopathological changes, Exp. Toxicol. Pathol. 64 (2012) 197–203, https://doi.org/10.1016/j.etp.2010.08.006.

[8] K. Shekhawat, S. Chatterjee, B. Joshi, Chromium toxicity and its health hazards, Int. J. Adv. Res. 3 (2015) 167–172.

[9] E. Denkhaus, K. Salnikow, Nickel essentiality, toxicity, and carcinogenicity, Crit. Rev. Oncol. Hematol. 42 (2002) 35–56, https://doi.org/10.1016/S1040-8428(01)00214-1.

[10] M. Jovaní, M. Fortuño-Morte, H. Beltrán-Mir, E. Cordoncillo, Environmental-friendly red-orange ceramic pigment based on Pr and Fe co-doped $Y_2Zr_2O_7$, J. Eur. Ceram. Soc. 38 (2018) 2210–2217, https://doi.org/10.1016/j.jeurceramsoc.2017.12.005.

[11] M. Fortuño-Morte, H. Beltrán-Mir, E. Cordoncillo, Study of the role of praseodymium and iron in an environment-friendly reddish orange pigment based on Fe doped $Pr_2Zr_2O_7$: a multifunctional material, J. Alloys Compd. 845 (2020), 155841, https://doi.org/10.1016/j.jallcom.2020.155841.

[12] M. Fortuño-Morte, P. Serna-Gallén, H. Beltrán-Mir, E. Cordoncillo, A new series of environment-friendly reddish inorganic pigments based on $AFeO_3$ (A = *Ln*, Y) with high NIR solar reflectance, J. Materiomic. 7 (2021) 1061–1073, https://doi.org/10.1016/j.jmat.2021.02.002.

[13] M. Ye, A. Han, Z. Chu, J. Che, C. Wang, Synthesis and characterization of Mn-doped copper chromite black pigments, Adv. Mater. Res. 602–604 (2013) 71–75. 10.4028/www.scientific.net/AMR.602-604.71.

[14] M. Dondi, C. Zanelli, M. Ardit, G. Cruciani, L. Mantovani, M. Tribaudino, G. B. Andreozzi, Ni-free, black ceramic pigments based on Co - Cr - Fe - Mn spinels: a reappraisal of crystal structure, colour and technological behaviour, Ceram. Int. 39 (2013) 9533–9547, https://doi.org/10.1016/j.ceramint.2013.05.072.

[15] O.O. Vasil'kov, O.P. Barinova, S.v. Kirsanova, N.A. Marnautov, A.B. Elfimov, Ceramic black pigments based on chromium-nickel spinel $NiCr_2O_4$, Glass Ceram. 74 (2017) 236–239, https://doi.org/10.1007/s10717-017-9970-8.

[16] D. Melo, F.T.G. Vieira, T.C.C. Costa, L.E.B. Soledade, C.A. Paskocimas, D.M. A. Melo, E. Longo, E.P. Marinho, A.G. Souza, I.M.G. Santos, Lanthanum cobaltite black pigments with perovskite structure, Dyes Pigments 98 (2013) 459–463, https://doi.org/10.1016/j.dyepig.2013.03.012.

[17] R. Oka, T. Masui, Synthesis and characterization of black pigments based on calcium manganese oxides for high near-infrared (NIR) reflectance, RSC Adv. 6 (2016) 90952–90957, https://doi.org/10.1039/c6ra21443f.

[18] R. Oka, S. Iwasaki, T. Masui, Improvement of near-infrared (NIR) reflectivity and black color tone by doping Zn^{2+} into the $Ca_2Mn_{0.85}Ti_{0.15}O_4$ structure, RSC Adv. 9 (2019) 38822–38827, https://doi.org/10.1039/c9ra07849e.

[19] M. Suwan, N. Sangwong, S. Supothina, Effect of Co and Pr doping on the properties of solar-reflective $ZnFe_2O_4$ dark pigment, IOP Conf. Ser. Mater. Sci. Eng. 182 (2017), 012003, https://doi.org/10.1088/1742-6596/755/1/011001.

[20] T. Fujimura, N. Sanefuji, K. Kataoka, Near Infrared-Reflective Black Pigment and Method for Producing Same, 2020.

[21] G. Monrós, S. Cerro, J.A. Badenes, M. Llusar, Black cool pigments for urban heat island (UHI) control: from Cr-hematite to Mn-melilite, J. Solar. Energy Res. Update. 8 (2021) 27–44.

[22] Y.G. Yang, J.H. Xu, B. Cai, Q.C. Wang, D.P. Xiu, Z.B. Zhao, Q.Z. Sun, S.L. Cao, Synthesis and applications of black ceramic from recycled industrial wastes, Adv. Appl. Ceramic. 112 (2013) 146–148, https://doi.org/10.1179/1743676112Y.0000000047.

[23] Z. Chen, Y. Du, Z. Li, D. Sun, C. Zhu, Synthesis of black pigments containing chromium from leather sludge, Ceram. Int. 41 (2015) 9455–9460, https://doi.org/10.1016/j.ceramint.2015.04.001.

[24] R. Zhu, G. Ma, Y. Cai, Y. Chen, T. Yang, B. Duan, Z. Xue, Ceramic tiles with black pigment made from stainless steel plant dust: physical properties and long-term leaching behavior of heavy metals, J. Air Waste Manag. Assoc. 66 (2016) 402–411, https://doi.org/10.1080/10962247.2016.1140096.

[25] M. Du, Y. Du, Z. Chen, Z. Li, K. Yang, X. Lv, Y. Feng, Synthesis and characterization of black ceramic pigments by recycling of two hazardous wastes, Appl. Phys. Mater. Sci. Process 123 (2017) 1–7, https://doi.org/10.1007/s00339-017-1181-1.

[26] C. Gargori, S.R. Prim, M. LLusar, M.v. Folgueras, G. Monrós, Recycling of Cr/Ni/Cu plating wastes as black ceramic pigments, Mater. Lett. 218 (2018) 341–345, https://doi.org/10.1016/j.matlet.2018.02.047.

[27] Q. Shen, S. Li, G. Yang, B. Sunden, J. Yuan, Effect of *A*-/*B*-site doping on oxygen non-stoichiometry, structure characteristics, and O_2 releasing behavior of $La_{1-x}Ca_xCo_{1-y}Fe_yO_{3-\delta}$ perovskites, Energies 12 (2019) 410, https://doi.org/10.3390/en12030410.

[28] J. Saha, Y.M. Jana, G.D. Mukherjee, R. Mondal, S. Kumar, H.C. Gupta, Structure, Mössbauer spectroscopy and vibration phonon spectra in valence-bond force-field model approach for distorted perovskites $AFeO_3$ (A = La, Y), Mater. Chem. Phys. 240 (2020), 122286, https://doi.org/10.1016/j.matchemphys.2019.122286.

[29] R.D. Shannon, Revised effective ionic radii and systematic studies of interatomie distances in halides and chalcogenides, Acta Crystallogr. A32 (1976) 751. http://journals.iucr.org/a/issues/1976/05/00/a12967/a12967.pdf.

[30] Y.Q. Jia, Crystal radii and effective ionic radii of the rare earth ions, J. Solid State Chem. 95 (1991) 184–187, https://doi.org/10.1016/0022-4596(91)90388-X.

[31] F. Zaza, V. Pallozzi, E. Serra, M. Pasquali, Combustion synthesis of $LaFeO_3$ sensing nanomaterial, in: AIP Conference Proceedings, 2015, pp. 1–11, https://doi.org/10.1063/1.4922559, 020003.

[32] M. Hepting, Ordering Phenomena in Rare-Earth Nickelate Heterostructures, Springer, 2017.

[33] S. Gupta, R. Medwal, S.P. Pavunny, D. Sanchez, R.S. Katiyar, Temperature dependent Raman scattering and electronic transitions in rare earth $SmFeO_3$, Ceram. Int. 44 (2018) 4198–4203, https://doi.org/10.1016/j.ceramint.2017.11.223.

[34] F. Ahmad Mir, M. Ikram, R. Kumar, Temperature-dependent Raman study of $PrFeO_3$ thin film, J. Raman Spectrosc. 42 (2011) 201–208, https://doi.org/10.1002/jrs.2655.

[35] A. Ruffo, M.C. Mozzati, B. Albini, P. Galinetto, M. Bini, Role of non-magnetic dopants (Ca, Mg) in $GdFeO_3$ perovskite nanoparticles obtained by different synthetic methods: structural, morphological and magnetic properties, J. Mater. Sci. Mater. Electron. 31 (2020) 18263–18277, https://doi.org/10.1007/s10854-020-04374-8.

[36] M.C. Weber, M. Guennou, H.J. Zhao, J. Íñiguez, R. Vilarinho, A. Almeida, J. A. Moreira, J. Kreisel, Raman spectroscopy of rare-earth orthoferrites $RFeO_3$ (R = La, Sm, Eu, Gd, Tb, Dy), Phys. Rev. B 94 (2016), 214103, https://doi.org/10.1103/PhysRevB.94.214103.

[37] K. Sultan, M. Ikram, K. Asokan, Structural, optical and dielectric study of Mn doped $PrFeO_3$ ceramics, Vacuum 99 (2014) 251–258, https://doi.org/10.1016/j.vacuum.2013.06.014.

[38] S. Shravan Kumar Reddy, N. Raju, Ch Gopal Reddy, P. Yadagiri Reddy, K. Rama Reddy, S.M. Gupta, V. Raghavendra Reddy, Study of Mn doped multiferroic $DyFeO_3$ ceramics, Ceram. Int. 43 (2017) 6148–6155.

[39] T. Yamashita, P. Hayes, Analysis of XPS spectra of Fe^{2+} and Fe^{3+} ions in oxide materials, Appl. Surf. Sci. 254 (2008) 2441–2449, https://doi.org/10.1016/j.apsusc.2007.09.063.

[40] Y. Li, Y. Ma, W. Liu, Z. Wang, H. Liu, X. Wang, H. Wei, S. Zeng, N. Yi, G.J. Cheng, A promising inorganic $YFeO_3$ pigments with high near-infrared reflectance and infrared emission, Sol. Energy 226 (2021) 180–191, https://doi.org/10.1016/j.solener.2021.08.047.

[41] A. Mekki, M. Salim, XPS study of transition metal doped silicate glasses, J. Electron. Spectrosc. Relat. Phenom. 101 (1999) 227–232, https://doi.org/10.1016/S0368-2048(98)00450-2.

[42] A. Mekki, D. Holland, C.F. McConville, M. Salim, An XPS study of iron sodium silicate glass surfaces, J. Non-Cryst. Solids 208 (1996) 267–276, https://doi.org/10.1016/S0022-3093(96)00523-6.

[43] F. Matteucci, G. Cruciani, M. Dondi, G. Gasparotto, D.M. Tobaldi, Crystal structure, optical properties and colouring performance of karrooite $MgTi_2O_5$ ceramic pigments, J. Solid State Chem. 180 (2007) 3196–3210, https://doi.org/10.1016/j.jssc.2007.08.029.

[44] K. Binnemans, C. Görller-Walrand, On the color of the trivalent lanthanide ions, Chem. Phys. Lett. 235 (1995) 163–174, https://doi.org/10.1016/0009-2614(95)00126-O.

[45] G. Monrós, Scheelite and Zircon: Brightness, Color and NIR Reflectance in Ceramics, Nova Science Publishers, New York, 2021.

[46] A.S. Teja, P.Y. Koh, Synthesis, properties, and applications of magnetic iron oxide nanoparticles, Prog. Cryst. Growth Char. Mater. 55 (2009) 22–45, https://doi.org/10.1016/j.pcrysgrow.2008.08.003.

[47] J. Mazo-Zuluaga, J. Restrepo, F. Muñoz, J. Mejía-López, Surface anisotropy, hysteretic, and magnetic properties of magnetite nanoparticles: a simulation study, in: Journal of Applied Physics, 2009, https://doi.org/10.1063/1.3148865.